

# At-Surface Reflectance and Albedo from Satellite for Operational Calculation of Land Surface Energy Balance

Masahiro Tasumi<sup>1</sup>; Richard G. Allen<sup>2</sup>; and Ricardo Trezza<sup>3</sup>

**Abstract:** This paper presents a rapid, operational method for estimating at-surface albedo applicable to Landsat and MODIS satellite sensors for typical cloud-free, low-haze conditions and sensor view angles less than 20°. At-surface albedo estimates are required input to various surface energy balance models that are applied operationally. The albedo calculation method was developed using the SMARTS2 radiative transfer model and has been applied in recent versions of the University of Idaho METRIC model as a component of the surface energy balance for determining evapotranspiration. The albedo procedure uses atmospheric correction functions developed to require only general humidity data and a digital elevation model. The atmospheric correction functions have a reduced structure to enhance their operational applicability in routine instantaneous surface energy balances and to estimate evapotranspiration. The method does not require high levels of knowledge in atmospheric physics and radiation transfer processes, common to traditional radiation transfer models, which enhances their use by a broad range of agricultural and hydrologic scientists and engineers. The atmospheric correction and surface albedo estimation procedures are developed primarily for use with Landsat imagery, which does not have an official albedo product. However, the procedure is also applicable to MODIS imagery that has an official albedo product at the 1 km scale, for situations where full broadband albedo having 500 m resolution is needed, where albedo is needed for select days having small sensor view angles for reduction of pixel blurring, or where image striping or reflectance data fallout has occurred in the standard MODIS albedo product. Method results have been compared to literature values and independent data sets. Test applications against MODIS albedo products in New Mexico, Florida, and Idaho indicate that the expected error for actual albedo from the developed method is within the interval of  $-0.035$  to  $+0.033$  (95% confidence level), equivalent to a standard error of 0.017, over broad ranges in land surface elevation, humidity, and sun angle.

**DOI:** 10.1061/(ASCE)1084-0699(2008)13:2(51)

**CE Database subject headings:** Energy; Satellites; Evapotranspiration; Hydrology.

## Introduction

Landsat has been one of the primary operational earth observation satellites over the past three decades. With long-term historical image records and high spatial resolution of 30 m in the short wave bands and 60–120 m in the thermal band, Landsat thematic mapper (TM) and enhanced thematic mapper plus (ETM+) images have been widely utilized for both research and nonresearch purposes. The high resolution of Landsat makes this satellite highly valuable for agricultural and water resources management, where reflective and thermal information can be retrieved for individual agricultural fields. On the other hand, the moderate-resolution imaging spectroradiometer (MODIS) on board the Terra and Aqua satellites is a relatively new, but coarser, sensor, available since 1999. Because MODIS produces highly automated, low-cost images having relatively frequent, albeit coarser

coverage than Landsat, MODIS images have become widely used for earth observation at the moderate spatial resolution of 250–1000 m.

Solar energy reflected from the earth's surface, as observed by satellite, is impacted by attenuation and scattering by the atmosphere between the satellite sensor and the surface target. The atmospheric effect must be eliminated during calculation of surface reflectance and albedo (albedo represents the broadband reflectance over the entire shortwave spectrum) and for land surface energy balance computations. Radiation transfer models (RTMs) are generally accepted for atmospheric correction of reflected radiation (Staeenz et al. 2002). Application of RTM, for example the MODTRAN model (Berk et al. 1999), is common in research applications that require high accuracy of at-surface reflectance and integrated albedo. In operational modes of atmospheric correction, the related 6S RTM (Vermote et al. 1997) is commonly applied, and is more computationally efficient than MODTRAN (e.g., Zhao et al. 2000). However, application of these RTM's in routine energy balance computations by public water management agencies, for example, the Idaho Department Water Resources that routinely applies the METRIC satellite-based evapotranspiration (ET) model (Kramber 2002; Allen et al. 2005, 2007a), is not popular for two reasons. First, extensive computational requirements of most RTM's involve the creation of lookup tables for standard atmospheric conditions to enable quick atmospheric correction (Liang et al. 2001). Second, ET and energy balance model operators may not have sufficient theoretical background and training to manipulate RTMs, since many operators are hydrologists, engineers, or GIS spatial analysts by training.

<sup>1</sup>Associate Professor, University of Miyazaki, 1-1, Gakuen Kibanadai-Nishi, Miyazaki 889-2192, Japan. E-mail: tasumi@cc.miyazaki-u.ac.jp

<sup>2</sup>Professor, Kimberly Research Center, University of Idaho, 3793 N 3600 E., Kimberly, ID 83341. E-mail: rallen@kimberly.uidaho.edu

<sup>3</sup>Visiting Associate Professor, University of Idaho, 3793 N. 3600 E., Kimberly, ID 83341. E-mail: rtrezza@kimberly.uidaho.edu

Note. Discussion open until July 1, 2008. Separate discussions must be submitted for individual papers. To extend the closing date by one month, a written request must be filed with the ASCE Managing Editor. The manuscript for this paper was submitted for review and possible publication on May 8, 2006; approved on October 31, 2006. This paper is part of the *Journal of Hydrologic Engineering*, Vol. 13, No. 2, February 1, 2008. ©ASCE, ISSN 1084-0699/2008/2-51-63/\$25.00.

Due to these challenges for operational application of RTM, simple, empirical atmospheric corrections have been developed and frequently used during processing of Landsat images (Moran et al. 2001; Liang et al. 2001, 2002a). The traditional dark-object subtraction (DOS) method and its several improved versions (e.g., Chavez 1988; Teillet and Fedosejevs 1995) provides simple, image-based correction for effects of haze on radiative attenuation. These techniques are most widely applied in operational aspects because of the convenience, even though the accuracy is often considered to be unacceptable for surfaces having reflectances of 0.15 or higher (Chavez 1996). The empirical line method overcomes the problem of DOS by utilizing an additional calibration point in a high-reflectance area. The method is considered to have sufficient accuracy for many applications (Smith and Milton 1999; Ben-Dor et al. 2004). However, the method requires one (bright) or two (bright and dark) known ground calibration targets, which can prove to be a constraint for application to large regions and for applications involving historical images. Liang et al. (2001, 2002a) developed a relatively rapid atmospheric correction model for Landsat ETM+ that corrected for heterogeneous aerosol scattering and surface adjacency effects. The model utilized histogram matching of reflectances for specific image calibration and to remove effects of haze and thin clouds and their shadows. The method is operationally applicable to a wide range of surface and atmospheric conditions. However, the method requires users to evaluate and optimize the procedures for identifying nonhazy regions and to specify the magnitude of a low-pass filter.

For MODIS images, calculated surface reflectances and albedo images have been distributed through NASA/USGS (Schaaf et al. 2002). However, corrected albedo products are available for 16-day periods only, and have a minimum of 1 km resolution rather than the 500-m resolution of the original MODIS short-wave image. In addition, several problems, including artifact stripes in images, have been reported for MODIS reflectance and albedo products (NASA 2005). Perhaps even more importantly for agricultural applications, the inclusion in the 16-day MODIS albedo product of reflectances from areas of images having large view angles causes substantial smearing of the final product, so that the effective pixel resolution increases from the stated 1 km, in reality, to approximately 2 km  $\times$  3 km. The effects of the smearing in the albedo product are profound when sampling albedo (and associated derived ET products) for individual agricultural fields or small land use areas. Therefore, independent calculation of surface reflectance and albedo is, typically, required with MODIS imagery when albedo for individual days having small sensor view angle and thus highest spatial resolution are obtainable.

The surface albedo estimation method presented in this paper was developed to improve the accuracy of net radiation components in commonly applied instantaneous surface energy balance and ET estimation models including SEBAL (Bastiaanssen et al. 1998; 2005; Bastiaanssen, 2000), METRIC (Allen et al. 2007b), SEBI (Roerink et al. 2000), and SEBS (Su 2002; Jia et al. 2003). The method attempts to reproduce RTM-based atmospheric corrections using a reduced equation format introduced by Majumdar et al. (1972) for atmospheric transmittance of global solar beam radiation that was adopted by the Food and Agricultural Organization (FAO) of the United Nations and the Environmental and Water Resources Institute (EWRI) of the American Society of Civil Engineers guidelines for standardized calculation of reference evapotranspiration (Allen et al. 1998; EWRI 2005). Unlike the majority of empirical and semiempirical methods, our method

is not image based. By limiting applications of the method to clear-sky and low-haze conditions (horizontal visibility  $>$   $\sim$  12 km), the method appears to be applicable with little expert decision making by operators, thereby equipping agricultural and hydrologic engineers with the capability to perform needed atmospheric corrections with reasonable accuracy for input to evapotranspiration models. The method uses an estimate of precipitable water in the atmosphere that is produced from MODIS satellite-based profiles or estimated, as a second alternative, from surface humidity data only. The low data requirement allows application in developing countries where detailed atmospheric parameters and data required by more-sophisticated models are not widely available. The method does not require ground calibration targets, and therefore, can be used in historical and regional studies.

In this study, two official MODIS reflectance and albedo products, MOD09 and MOD43 (Vermote and Vermeulen 1999; Schaaf et al. 2002) were used for comparison with model estimates and to develop calibrations for the small path reflectance terms. The MOD09 product constitutes at-surface band reflectance, which is predominantly, but not entirely, bidirectional (BD). The MOD09 reflectance products were integrated to broadband albedo during this study for comparison with our calculated at-surface albedo. In addition, actual surface albedo calculated using the MOD43B1 16-day albedo product was used as an additional reference basis for comparing with our estimated at-surface albedo. Actual at-surface albedo, which is predominately directional-hemispherical, is more important in surface energy balance computations than the predominantly BD albedo derived from integration of the MOD09 product because it is a truer representation of albedo integrated over all directions. For near-nadir sensor view angles, however, differences are generally small. Preliminary evaluations by Liang et al. (2002b) showed that MOD09 and MOD43 reflectance and albedo products are reasonably accurate when the images are near-nadir and from clear-sky conditions. Liang et al. found error to average about 0.025 for all shortwave bands, with largest error (0.047) in MOD09 Band 5 and smallest error (0.002–0.006) in the MOD43 broadband albedo. Both MODIS products are derived using complex atmospheric correction algorithms that are traceable to the 6S model, which is in turn traceable to the MODTRAN correction procedure (Vermote and Vermeulen 1999; Schaaf et al. 2002). In this study, we carefully reviewed and avoided effects of sensor malfunctioning, and therefore, the MOD09 and MOD43 MODIS products were considered to be reliable tools for calibration and comparison.

### Traditional Albedo Estimation Methods in Operational Surface Energy Balance Models

In operational application of instantaneous surface energy balance models, only a limited number of applications have utilized precise atmospheric correction and albedo estimation (e.g., Ma et al. 2004) due to the physical and technical constraints previously discussed. Instead, many widely used and operationally applicable models such as SEBAL and SEBI have traditionally applied what may be considered to be overly simplified albedo computation strategies using equations similar to Eq. (1), where broadband at-surface albedo,  $\alpha_s$ , is estimated on a broad-spectrum basis (Bastiaanssen et al. 1998; Farah and Bastiaanssen 2001; Roerink et al. 2000; Tasumi et al. 2000):

$$\alpha_s = \frac{\alpha_t - \alpha_a}{\tau_{bb}^2} \quad (1)$$

where  $\alpha_t$ =at-satellite broadband bidirectional albedo;  $\alpha_a$ =atmospheric (path) induced albedo; and  $\tau_{bb}^2$ =two-way broadband atmospheric transmittance that assumes equal transmissivity for incoming and outgoing radiation.

The simple broadband method such as in Eq. (1) is beset by three problems. First, the concept of using a wide-spectrum or “broadband” transmittance is inappropriate for correction of discretely banded images, where Landsat TM/ETM+ and MODIS land observation sensors have been selectively designed to function in high-transparency spectral bands. Second, this method does not consider differences among atmospheric transmittances of individual sensor bands. Third, the integration of narrowband to broadband reflectance should be done using band weights that are proportional to the intensity of solar radiation at the surface (Starks et al. 1991), which is not commonly done with this method. Recent research indicates that application of Eq. (1) may underestimate net radiation as used in surface energy balance computations and resulting ET estimates over bright, bare soil surfaces by as much as 15% (Tasumi et al. 2005).

### New Albedo Estimation Method

The operational method developed here estimates surface albedo by separately calculating at-surface reflectance for each satellite sensor band and then integrating these reflectances according to intensities of at-surface solar radiation (incoming) within the domain of the band. The method does not correct for any bidirectional reflectance distribution caused by a substantial off-nadir sensor view angle, such as that occurring with MODIS at large scan angles, where shadowing within plant canopies or preferential forward reflection of the solar beam causes deviation in reflected signals to the sensor as compared to near nadir positioning. Therefore, the equations developed here are most applicable to near-nadir sensor view angles (within 0 to 20° of nadir, approximately) unless some type of bidirectional reflectance distribution function (BRDF) correction is applied. The method was developed for use with high-resolution (30 m) Landsat images and applications using near-nadir MODIS images where 500-m resolution albedo is desired.

The albedo calculation process comprises the following steps:

1. Calculation of at-satellite bidirectional reflectance from at-satellite radiance values assuming the absence of an atmosphere.
2. Calculation of at-surface reflectance from at-satellite BD reflectance values (i.e., application of atmospheric correction). The calculated at-surface reflectance is not entirely, but is predominately, BD reflectance, since it is calculated using information measured by the satellite sensor, which is a “directional” sensor. Whereas, at-surface solar radiation is a mixture of beam (i.e., directional) and diffuse (i.e., hemispherical) components, where the directional component is predominant under clear sky conditions.
3. Estimation of broadband surface albedo by integrating the at-surface band reflectances.

For Landsat images, the processing begins with Step 1. For MODIS images, the initial processing step depends on the product level of the MODIS image. Processing begins with Step 1 if Level 1 calibrated radiance is used as input, or from Step 3 if Level 2 daily surface reflectance is used as input. The detailed

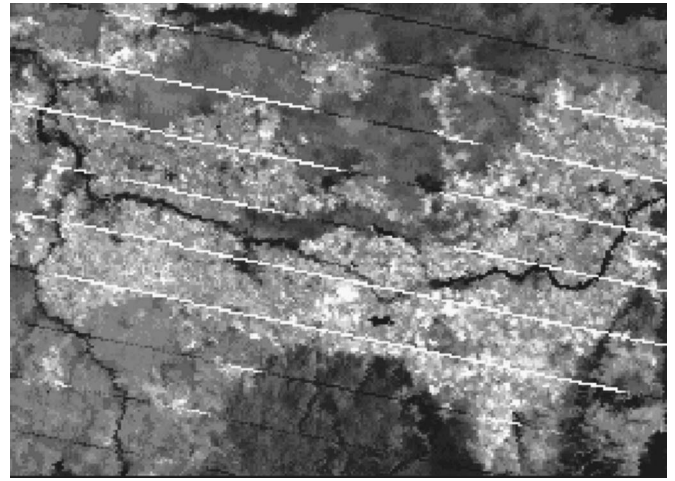


**Fig. 1.** Stripe in MOD09 surface reflectance Band 5, observed on August 9, 2004, in southern Idaho

method for Step 1 is found in Chander and Markham (2003) and LPSO (2006), with modifications for surface inclination of the landscape (Duffie and Beckman 1991; see the Appendix). The developed procedure utilizes Landsat TM/ETM+ Bands 1–5 and 7, or MODIS Bands 1–7. Integration weights applied in Step 3 must be modified if any of the suggested bands are rejected due to sensor malfunctioning, which is a common issue of MODIS images (NASA 2005; See Fig. 1, as an example). Modification of weights is straightforward with the developed weighting procedure.

### At-Surface Reflectance

In Step 2, at-surface reflectance is derived by correcting the at-satellite BD reflectance for scattering and absorption of incoming solar radiation and scattered reflected radiation from the surface. Exoatmospheric solar radiation must be converted to at-surface solar radiation, which is a mixture of directional and hemispherical components. This is done using a calibrated atmospheric transmittance function. At-satellite observed directional radiance is converted to at-surface reflected directional radiance using a combination of atmospheric transmittance function and path reflectance. In our procedure we have developed an atmospheric correction model that requires only an estimate of total precipitable water or, if that is unavailable, general humidity data.

The at-surface reflectance for band “b,”  $\rho_{s,b}$ , is calculated in our procedure as

$$\rho_{s,b} = \frac{R_{out,s,b}}{R_{in,s,b}} = \frac{\rho_{t,b} - \rho_{a,b}}{\tau_{in,b} \cdot \tau_{out,b}} \quad (2)$$

where  $R_{in,s,b}$  and  $R_{out,s,b}$ =mean at-surface incoming and reflected radiances within band  $b$  ( $\text{W m}^{-2} \mu\text{m}^{-1}$ ), and  $\tau_{in,b}$  and  $\tau_{out,b}$ =effective narrowband transmittances for incoming solar radiation and for shortwave radiation reflected from the surface in band  $b$ . Parameter  $\rho_{t,b}$ =at-satellite reflectance for band  $b$  calculated at the top of the atmosphere (See the Appendix), and  $\rho_{a,b}$  is an atmospheric path reflectance for band  $b$ .  $\tau_{in,b}$  and  $\tau_{out,b}$  account for attenuation of both beam and diffuse radiation and are calculated using individually derived equations for each band of the satellite.  $\rho_{a,b}$  is calculated for each band as a function of transmittance.



The transmittance functions for  $\tau_{in,b}$  and  $\tau_{out,b}$  follow a format similar to the broadband (global) transmittance function of Majumdar et al. (1972) that was adapted by FAO and EWRI standardizations for calculating evapotranspiration (Allen et al. 1998; EWRI 2005) and extended in this study to narrowband applications

$$\tau_{in,b} = C_1 \exp \left[ \frac{C_2 P_{air} - C_3 W - C_4}{\cos \theta} \right] + C_5 \quad (3)$$

where  $P_{air}$ =atmospheric pressure (kPa);  $\theta$ =solar zenith angle for horizontal surfaces;  $W$ =precipitable water in the atmosphere (mm); and  $C_1$ – $C_5$  are fitted satellite-dependent constants presented later in the calibration section.  $P_{air}/\cos \theta$ =surrogate for atmospheric mass and optical path length.

The solar zenith angle  $\theta$  in Eq. (3), which is relative to the perpendicular to a horizontal flat surface, is used even for applications in mountainous terrain to properly estimate relative atmospheric thickness. The original broadband transmissivity equation by Allen et al. (1998) and EWRI (2005), which has a similar form to Eq. (3), contains an atmospheric turbidity term that is difficult to calibrate for specific applications and was, therefore, dropped from the narrow band equations, which are, therefore, limited to low-haze conditions (horizontal visibility  $> \sim 12$  km). It is recognized that atmospheric transmissivity, and thus correction, is sensitive to aerosol levels (e.g., Wen et al., 1999). For high-haze images contaminated by mineral dust or anthropogenic pollutants, an image-based correction method should be applied. Horizontal visibility information is, typically, available from nearby airports.

Mean atmospheric pressure (kPa) is calculated following EWRI (2005) as

$$P_{air} = 101.3 \left( \frac{293 - 0.0065z}{293} \right)^{5.26} \quad (4)$$

where 293=standard air temperature (K) for agricultural conditions; and  $z$ =elevation above sea level (m).

MODIS total precipitable water maps, available in the MOD05 science product (Gao and Kaufman 1999) are recommended as a convenient source of data for  $W$ . The MODIS maps are available at 1 km spatial resolution. In the absence of profile-based information on  $W$ ,  $W$  can be calculated using measured or estimated near-surface vapor pressure from a representative weather station, for example, using the equation derived for North America by Garrison and Adler (1990)

$$W = 0.14 e_a P_{air} + 2.1 \quad (5)$$

where  $e_a$ =near-surface vapor pressure (kPa); and  $W$  is in millimeters.

Eq. (5) is utilized in standardized evapotranspiration computations by FAO (Allen et al., 1998) and EWRI (2005). However,  $W$  estimated by near-surface point measurement may not explain the spatial variability of  $W$  within a satellite image. If Eq. (5) is applied, the operator should use weather data that represent average weather conditions for the image.

Parameter  $\tau_{in,b}$  can vary from  $\tau_{out,b}$  due to impacts of backscattered diffuse radiation originating from radiation from the reflected surface that is contained in  $\tau_{in,b}$  but not in  $\tau_{out,b}$ . However, in this study, outgoing narrowband effective transmittance,  $\tau_{out,b}$ , was found to be sufficiently well approximated using the same coefficients as for incoming transmittance, but with equivalent atmospheric path length calculated for the angle between the land surface and sensor (i.e., satellite). Therefore, the cosine of the sensor view angle is used rather than solar zenith angle

$$\tau_{out,b} = C_1 \exp \left[ \frac{C_2 P_{air} - C_3 W - C_4}{\cos \eta} \right] + C_5 \quad (6)$$

where  $\eta$ =sensor view angle relative to the perpendicular from a flat, horizontal surface, which is zero for a nadir view and  $\pi/2$  rad for a horizontal view angle. Mean biases caused by real differences between  $\tau_{in,b}$  and  $\tau_{out,b}$  were incorporated into the  $\rho_{a,b}$  term of Eq. (3) during calibration.

Landsat has a near-nadir view angle, and thus,  $\cos \eta$  for the entire image can be assumed to be 1. MODIS image sensor angles vary each day, occasionally exceeding  $\pi/4$  rad ( $50^\circ$ ), and therefore,  $\eta$  changes by image date and with each pixel location. The sensor-dependent constants  $C_1$ – $C_5$  in Eqs. (3) and (6), and the atmospheric reflectance of each band,  $\rho_{a,b}$  in Eq. (2), were calibrated using radiative transfer models as described in a following section.

### Estimation of Broadband Surface Albedo by Integrating Narrowband At-Surface Reflectances

In Step 3, broadband surface albedo is calculated from multiband satellite data by integrating band reflectances across the short-wave spectrum. Here, we integrate at-surface band reflectance following Starks et al. (1991) where

$$\alpha_s = \sum_{b=1}^7 [\rho_{s,b} \cdot w_b] \quad (7)$$

where  $w_b$ =weighting coefficient representing the fraction of at-surface solar radiation occurring within the spectral range represented by a specific band

$$w_b = \frac{\int_{LO_b}^{UP_b} R_{s\lambda} \cdot d\lambda}{\int_{0.3}^{4.0} R_{s\lambda} \cdot d\lambda} \quad (8)$$

where  $R_{s\lambda}$ =at-surface spectral hemispherical solar radiation for wavelength  $\lambda$  ( $\mu\text{m}$ );  $UP_b$  and  $LO_b$ =upper- and lower-wavelength bounds ( $\mu\text{m}$ ) assigned to Landsat or MODIS band  $b$ , which, in our application, includes all regions between the specific satellite bands. Inclusion of wavelength regions between sensor bands in the determination of weighting provides a more theoretically correct estimate of total surface reflectance assuming that reflectance of regions between satellite bands can be approximated by linear interpolation of reflectances for neighboring bands. The regions between satellite bands were arbitrarily divided midway between band edges as shown in Table 1. Overall endpoints of integration were chosen as 0.3–4.0  $\mu\text{m}$ , which covers 98% of total at-surface solar radiation. For the MODIS band coefficients, only the first seven bands of MODIS were utilized since these represent significant regions of the broad spectrum, are similar to bands of Landsat, have native resolution of 500 m at sensor nadir, and are those used by MODIS albedo products (Schaaf et al. 2002). At-surface solar radiation is used for weighting rather than exoatmospheric radiation, as is sometimes done, because at-surface values account for the influence of atmospheric attenuation that varies with wavelength.

**Table 1.** Landsat and MODIS Band Widths and Ranges for  $LO_b$  and  $UP_b$  Applied in Eq. (8)

| Band | Band limits ( $\mu\text{m}$ ) |             | Applied $LO_b$ – $UP_b$ ( $\mu\text{m}$ ) |             |
|------|-------------------------------|-------------|---|-------------|
|      | Landsat <sup>a</sup>          | MODIS       | Landsat                                   | MODIS       |
| 1    | 0.45–0.52                     | 0.620–0.670 | 0.300–0.520                               | 0.593–0.756 |
| 2    | 0.52–0.60                     | 0.841–0.876 | 0.520–0.615                               | 0.756–1.053 |
| 3    | 0.63–0.69                     | 0.459–0.479 | 0.615–0.725                               | 0.300–0.512 |
| 4    | 0.76–0.90                     | 0.545–0.565 | 0.725–1.225                               | 0.512–0.593 |
| 5    | 1.55–1.75                     | 1.230–1.250 | 1.225–1.915                               | 1.053–1.439 |
| 6    | 10.4–12.5                     | 1.628–1.652 | Thermal                                   | 1.439–1.879 |
| 7    | 2.08–2.35                     | 2.105–2.155 | 1.915–4.000                               | 1.879–4.000 |

<sup>a</sup>Official band wavelength for Landsat 5TM. Band limits for Landsat 7 ETM+ are slightly different in the following bands: Band 2 (0.53–0.61); Band 4 (0.78–0.90); and Band 7 (2.09–2.35).

## Parameter Determination

The constants  $C_1$ – $C_5$  in Eqs. (3) and (6) were calibrated using the SMARTS2 radiative transfer model developed by Gueymard (1995). The SMARTS2 model has been distributed by the U.S. National Renewable Energy Laboratory (NREL) and provides spectral exoatmospheric and at-surface solar radiation over small band increments based on user-defined atmospheric and geometric conditions. SMARTS2 has been shown to compare closely with MODTRAN simulations over typical clear sky conditions (Gueymard 1995). Spectral transmittance for specific wavelength increments was obtained from model results by ratioing at-surface and exoatmospheric values.

SMARTS2 model simulations were made for 100 combinations of solar zenith angle, air water content, and land elevation for a hypothetical surface having uniform spectral reflectance of

0.2. The value 0.2 is commonly used in model runs representing agricultural settings and is used in the RTM to simulate backscatter of reflected radiation to the surface. The *U.S. Standard Atmosphere 1976* (NOAA/NASA/USAF 1976) was used to represent humidity and temperature profiles and aerosol conditions, with humidity profiles modified according to total precipitable water. Table 2 summarizes the ranges and increments evaluated for solar zenith angle, precipitable water and elevation ( $5 \times 5 \times 4 = 100$  combinations). These ranges represent a wide range of solar angles and atmospheric water vapor contents expected above both dry desert and humid terrain. Elevations ranged from sea level to that of tall mountains. The SMARTS2 outputs were used to calibrate  $C_1$ – $C_5$  using multiple regression, where the exponential term of Eq. (3) was regarded as a single variable,  $Y$ , with the equation expressed as a simple linear equation  $\tau_{in,b} = C_1 \cdot Y + C_5$ .  $C_2$ ,  $C_3$ , and  $C_4$  were selected to maximize the  $R$  square of the regression of  $Y$  versus  $\tau_{in,b}$  and parameters  $C_1$  and  $C_5$  were solved to force the final relationship to have slope=1 and intercept=0 relative to the original data.

Calibration constants are summarized in Table 3 for Landsat and in Table 4 for MODIS. Fig. 2 shows the calculated and predicted  $\tau_{in,b}$  for Landsat.  $R$ -square values exceeded 0.99 for each of the six Landsat bands and for each of the seven MODIS bands for the entire calibration data set. As evidenced in Fig. 2, the reduced model of Eq. (3), with the fitted calibration constants, closely reproduced the original SMARTS2 transmittances across the wide

**Table 2.** Levels of Solar Zenith Angle, Precipitable Water, and Location Elevation Evaluated during SMARTS2 Simulations

| Parameter                          | 1 | 2      | 3      | 4      | 5      |
|------------------------------------|---|--------|--------|--------|--------|
| Solar zenith angle, $\theta$ (rad) | 0 | 0.5548 | 0.7954 | 0.9884 | 1.1593 |
| Precipitable water, $W$ (mm)       | 3 | 5      | 12     | 40     | 60     |
| Elevation, $z$ (m)                 | 0 | 1,200  | 2,400  | 4,000  | —      |

**Table 3.** Calibrated Landsat Constants  $C_1$  to  $C_5$  for Eqs. (3) and (6) and  $C_b$  for  $\rho_{a,b}$  as Defined in Eq. (9)

| Coefficient | Band 1   | Band 2   | Band 3   | Band 4   | Band 5   | Band 7   |
|-------------|----------|----------|----------|----------|----------|----------|
| $C_1$       | 0.987    | 2.319    | 0.951    | 0.375    | 0.234    | 0.365    |
| $C_2$       | −0.00071 | −0.00016 | −0.00033 | −0.00048 | −0.00101 | −0.00097 |
| $C_3$       | 0.000036 | 0.000105 | 0.00028  | 0.005018 | 0.004336 | 0.004296 |
| $C_4$       | 0.0880   | 0.0437   | 0.0875   | 0.1355   | 0.0560   | 0.0155   |
| $C_5$       | 0.0789   | −1.2697  | 0.1014   | 0.6621   | 0.7757   | 0.639    |
| $C_b$       | 0.640    | 0.310    | 0.286    | 0.189    | 0.274    | −0.186   |

**Table 4.** Calibrated MODIS Constants  $C_1$ – $C_5$  for Eqs. (3) and (6) and  $C_b$  for  $\rho_{a,b}$  as Defined in Eq. (9)

| Coefficient | Band 1   | Band 2   | Band 3   | Band 4   | Band 5   | Band 6   | Band 7   |
|-------------|----------|----------|----------|----------|----------|----------|----------|
| $C_1$       | 1.102    | 0.451    | 0.996    | 1.944    | 0.318    | 0.216    | 0.275    |
| $C_2$       | −0.00023 | −0.00023 | −0.00071 | −0.00016 | −0.00022 | −0.00050 | −0.00031 |
| $C_3$       | 0.000290 | 0.000550 | 0.000036 | 0.000105 | 0.000640 | 0.000800 | 0.004296 |
| $C_4$       | 0.0875   | 0.0900   | 0.0880   | 0.0540   | 0.0760   | 0.0940   | 0.0155   |
| $C_5$       | −0.0471  | 0.5875   | 0.0678   | −0.8870  | 0.7100   | 0.8006   | 0.7282   |
| $C_b$       | 0.262    | 0.397    | 0.679    | 0.343    | 0.680    | 0.639    | −0.464   |

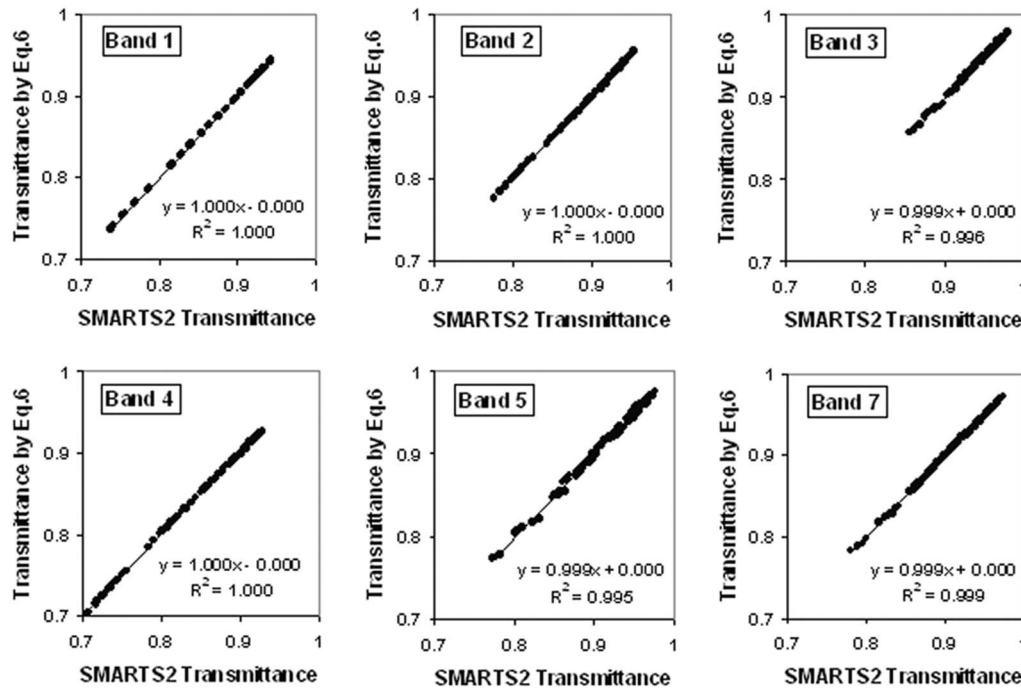


**Fig. 2.** Comparison of transmittance for Landsat bands estimated by Eq. (3) versus transmittance simulated by SMARTS2 for 100 combinations of sun angle, precipitable water, and land elevation

range of parametric values. The high  $R$ -square values indicate that the relatively simple format of Eq. (3) is appropriate to explain the behavior of atmospheric correction as simulated by SMARTS2 for the given standard atmosphere over the wide range of elevation, humidity and solar zenith angles investigated.

Analyses indicate that the transmittances estimated by Eqs. (3) and (6) are insensitive to assumptions concerning the specific atmospheric profiles defined by Anderson et al. (1986) and NOAA/NASA/USAF (1976) used with SMARTS2 during calibration. For example, at the broadband level, there are no differences between estimates by the calibrated model [based on the *U.S. Standard Atmosphere 1976* (NOAA/NASA/USAF 1976)] and those by SMARTS2 applied using the standard arctic atmosphere, and only 0.5% difference when SMARTS2 is operated using the standard tropic atmosphere. Differences are small partly because we specify precipitable water and pressure using actual humidity and elevation data in both models. However, the small differences do indicate general insensitivities to assumptions regarding other atmospheric constituents and specific profile shapes for water vapor.

After the transmittance equations were calibrated, atmospheric path reflectance,  $\rho_{a,b}$ , was back calculated for each band by inverting Eq. (2) using the MODIS (MOD02) calibrated radiance product to represent  $\rho_{t,b}$ , using the MODIS at-surface reflectance product MOD09 as the reference  $\rho_{s,b}$ , and using  $\tau_{in,b}$  and  $\tau_{out,b}$  from Eqs. (3) and (6). The inverted Eq. (2) was applied to a long series of sampled pixels from a near-nadir, clear-sky MODIS image over Idaho acquired on August 9, 2004. Values derived for  $\rho_{a,b}$  were numerically stable and essentially constant within each band over a wide range of surface reflectances. Values for  $\rho_{a,b}$  ranged from less than 0.01 (near-infrared bands) to 0.08 (blue band) across the seven bands of MODIS. The nearly constant values derived for  $\rho_{a,b}$  over the wide ranges of surface reflectance tested indicates relatively accurate calibration of the  $\tau_{in,b}$  and  $\tau_{out,b}$  functions. Following the calibration of  $\rho_{a,b}$  values, functions for

$\rho_{a,b}$  were parametrized to approximate  $\rho_{a,b}$  under other atmospheric and sun angle conditions by proportioning them to the estimated amount of one-way scattered and absorbed radiation as represented by  $1 - \tau_{in,b}$ , which is the potential source for  $\rho_{a,b}$

$$\rho_{a,b} = C_b(1 - \tau_{in,b}) \quad (9)$$

where  $C_b$ =determined scaling ratio for band “b.”

Coefficients for determining  $\rho_{a,b}$  for use with Landsat were derived using  $\rho_{a,b}$  from MODIS assuming that the estimates for  $\rho_{a,b}$ , if unbiased, are physical functions of the atmosphere, only, and are therefore applicable across satellite platforms. Therefore, coefficients for Landsat were calculated by interpolating MODIS  $\rho_{a,b}$  coefficients within and among commonly associated bands.

The calibrated coefficients,  $C_b$ , for Eq. (9) are summarized in Tables 3 and 4 for Landsat and MODIS, respectively. The negative values for Band 7 of both Landsat and MODIS indicate some residual calibration error in  $\tau_{in,b}$ . The  $C_b$  value for Band 7 of both Landsat and MODIS is very sensitive to small errors during calibration, because these midinfrared bands represent less than 4% of extraterrestrial solar radiation energy, and atmospheric transmittance in these bands is high. Thus,  $C_b$  for Band 7 is determined by dividing one small number by another. We have elected to retain the negative values for  $C_b$ , because the absolute error in total albedo caused by error in  $\rho_{a,b}$  for Band 7 is on the order of only 0.001.

Fig. 3 compares at-surface reflectances calculated with our atmospheric correction equations to those from MOD09 for 50 sampled pixels from the August 9, 2004, calibration image from Idaho. Our calculated values utilized a MODIS radiance image from the MOD02 product to calculate  $\rho_{t,b}$  and applied Eqs. (2), (3), (6), and (9) using the constants in Table 4. Land areas that had nearly uniform soil and vegetation characteristics were sampled to avoid error introduced by georegistration inconsistencies between the two MODIS products. Comparisons at the

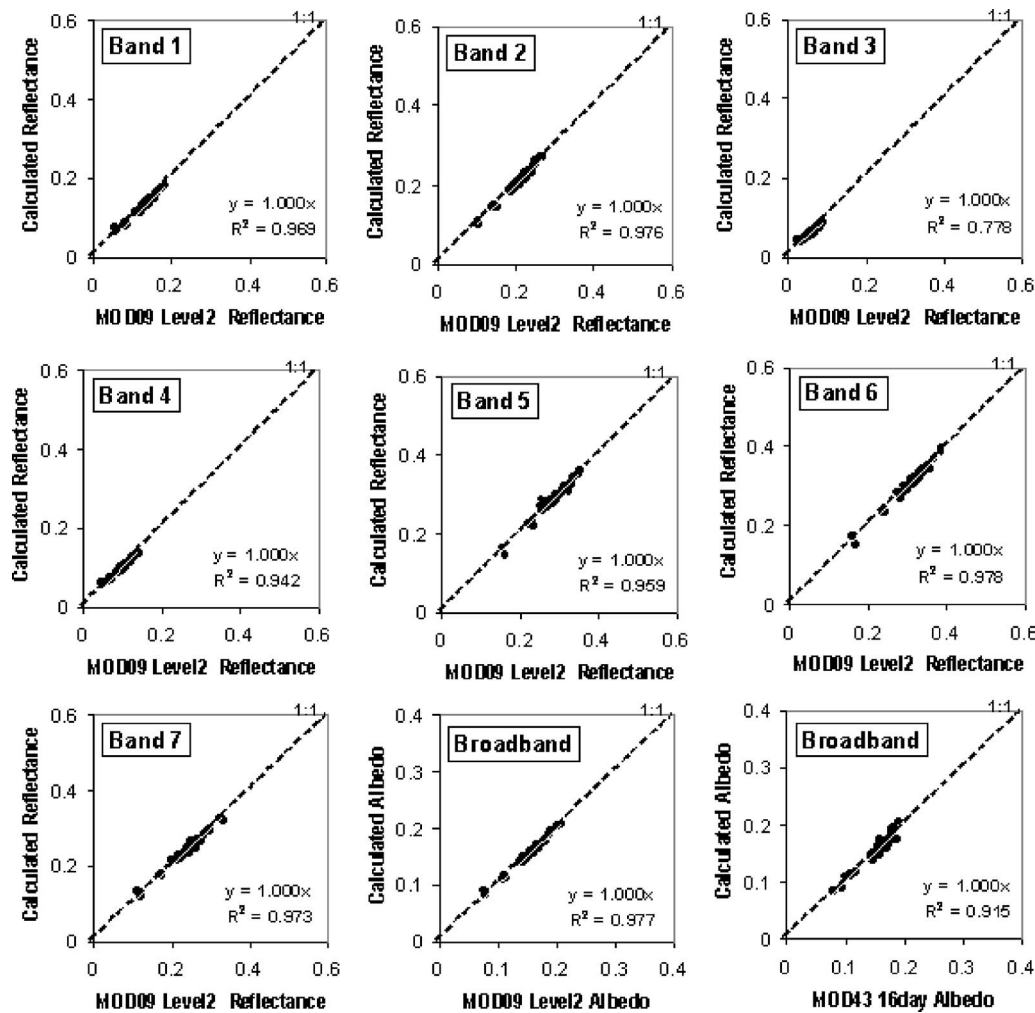


**Fig. 3.** Estimated at-surface reflectance for a MODIS Terra image on August 9, 2004, for 50 homogeneous sample surfaces over southern Idaho [based on Eqs. (3)–(5)], compared with the MODIS Level 2 surface reflectance and Level 3 albedo products

broadband level are also shown in Fig. 3, where broadband albedo was calculated from both our model and from the MOD09 Level 2 reflectance product using Eq. (7) for integration (the latter broadband albedo calculation is termed MOD09 albedo in Fig. 3). In addition, the comparative basis for the last graph in Fig. 3 is the MOD43 broadband albedo product representing the 16-day period encompassing August 9, 2004. Values for  $C_b$  in Table 4 were calibrated using this image by constructing regression lines in Fig. 3 having slope of 1.00 and intercept forced to zero. The strong linearity between calculated and MOD09 reflectances is a strong indication of successful calibration.

The weighting coefficients,  $w_b$ , used in Eq. (7) were determined using at-surface spectral data representing clear sky conditions. As defined by Eq. (8),  $w_b$  is strongly related to the relative intensities of at-surface solar radiation in the various bands and relative positioning of the bands. Our analyses show that variation in solar radiation with latitude and time occurs in nearly the same proportion across all bands, and thus, values for  $w_b$  are very stable over a wide range of solar radiation intensities and solar angles. Fig. 4 shows at-surface solar radiation levels derived from SMARTS2 and calculated  $w_b$  for one typical and two extreme combinations of land elevation, precipitable water, and solar angle:

- Case 1:  $z=870$  m,  $W=12$  mm, and  $\theta=0.66$  rad ( $38^\circ$ ) (a typical setting for Landsat images in southern Idaho).
- Case 2:  $z=4000$  m,  $W=3$  mm, and  $\theta=0$  rad. (an extremely transparent atmosphere).
- Case 3:  $z=0$  m,  $W=60$  mm, and  $\theta=1.16$  rad. ( $66^\circ$ ) (a relatively low transmittant atmosphere).

As shown in Figure 4,  $w_b$  did not change measurably over the wide range of solar radiation settings. Thus, we propose using fixed  $w_b$  values from Case 1 for all low-haze atmospheric conditions and for all latitude, time, land elevation and atmospheric water contents. The values for Case 1 are listed in Table 5.

## Validation of the Developed Method

### Comparison of Atmospheric Correction with MODIS Products

Reflectances and albedo estimated using MODIS Level 1 calibrated radiance data as input to Eqs. (2), (3), (6), and (7) are compared here against the MODIS official surface reflectance and albedo products for southern Idaho and New Mexico as tests under dry atmospheric conditions ( $W$  ranged from about



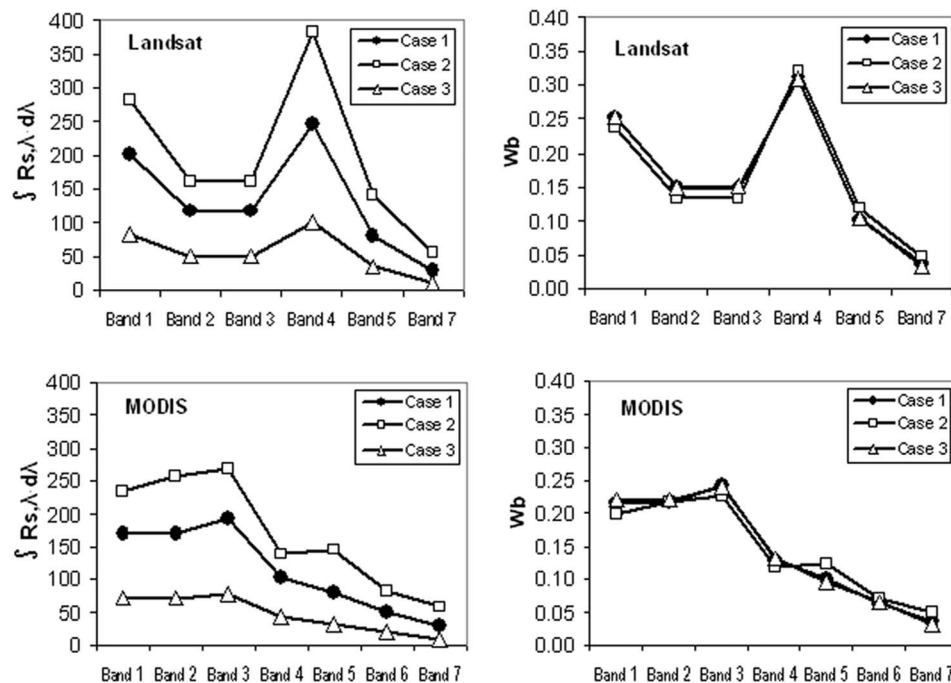


Fig. 4. Within-band solar radiation and  $w_b$  for three solar radiation conditions for Landsat and MODIS shortwave bands

5 to 10 mm), and for Florida as a test under humid atmospheric conditions ( $W$  ranged from about 12 to 25 mm). In the Idaho test, an additional comparison was made for an image having large sensor view angle ( $35\text{--}42^\circ$ ), which is significantly greater than our recommended application limit of  $20^\circ$ . Table 6 summarizes characteristics of the MODIS images processed for calibration and comparison, including the sensor view angle (from zenith), sample numbers and conditions of the sampled pixels. Sampled pixels were selected from among relatively homogeneous surfaces to reduce error caused by georegistration differences between MODIS products, especially for the BRDF albedo product, which is a 1 km resolution product having composited information from a large number of view angles (composited days) that causes smearing and makes its effective resolution larger than 1 km.

Fig. 5 compares band by band reflectance and computed albedo estimates from the model against reflectances from the MOD09 and albedo from the MOD43 products. The prediction confidence interval (at 95% confidence) was calculated using

standard procedures (Berthouex and Brown 1994) and was based on all samples from the three normal test applications. The prediction limits are indicated in Fig. 5. The slopes and intercepts of the linear regressions for each test application are summarized in Table 7. The slopes determined for Band 3 were numerically unstable (1.17 for Test-3 and 0.87 for Test EX) due to the small variability in sampled surface reflectance for this band. However, Fig. 5 suggests that all samples in the Band 3 comparison lie relatively close to a 1:1 line. The results in Fig. 5 and Table 7 show that surface reflectances calculated using our model agree closely with the official MODIS products over wide ranges of reflectance in each band and over the wide range of conditions represented by the three locations. Maximum error between estimated and MOD09 produced reflectances were  $-0.037$  (Band 6) and  $+0.034$  (Band 5) for surface reflectance intensities of 0.2 (95% confidence). The generally good agreement between band reflectances indicate that the atmospheric corrections made using the relatively simple Eqs. (2), (3), and (6) produce nearly the same correction as applied in developing the MOD09 surface

Table 5. Weighting Coefficients Based on At-Surface Solar Radiation Derived from SMARTS2

| Satellite | Band 1 | Band 2 | Band 3 | Band 4 | Band 5 | Band 6 | Band 7 | Total |
|-----------|--------|--------|--------|--------|--------|--------|--------|-------|
| Landsat   | 0.254  | 0.149  | 0.147  | 0.311  | 0.103  | —      | 0.036  | 1.000 |
| MODIS     | 0.215  | 0.215  | 0.242  | 0.129  | 0.101  | 0.062  | 0.036  | 1.000 |

Table 6. Summary Description of MODIS Images Used for Five Tests of Reflectance Model Applications

| Image number | Purpose                           | Date           | Sensor Zenith (degrees) | Number of samples | Conditions of samples                             |
|--------------|-----------------------------------|----------------|-------------------------|-------------------|---|
| 1            | Calibration (Idaho)               | August 9, 2004 | 0–6                     | 50                | From wide-open homogeneous desert bare soils      |
| 2            | Test 1 (Idaho)                    | August 7, 2004 | 16–27                   | 65                | Homogeneous bare soils, heterogeneous agriculture |
| 3            | Test 2 (New Mexico)               | April 4, 2002  | 0–23                    | 48                | Homogeneous bare soils, basalt and snow           |
| 4            | Test 3 (Florida)                  | May 4, 2004    | 0–10                    | 38                | Relatively homogeneous natural vegetations        |
| 5            | Test EX (Idaho, off sensor-angle) | August 5, 2004 | 35–42                   | 65                | Homogeneous bare soils, heterogeneous agriculture |



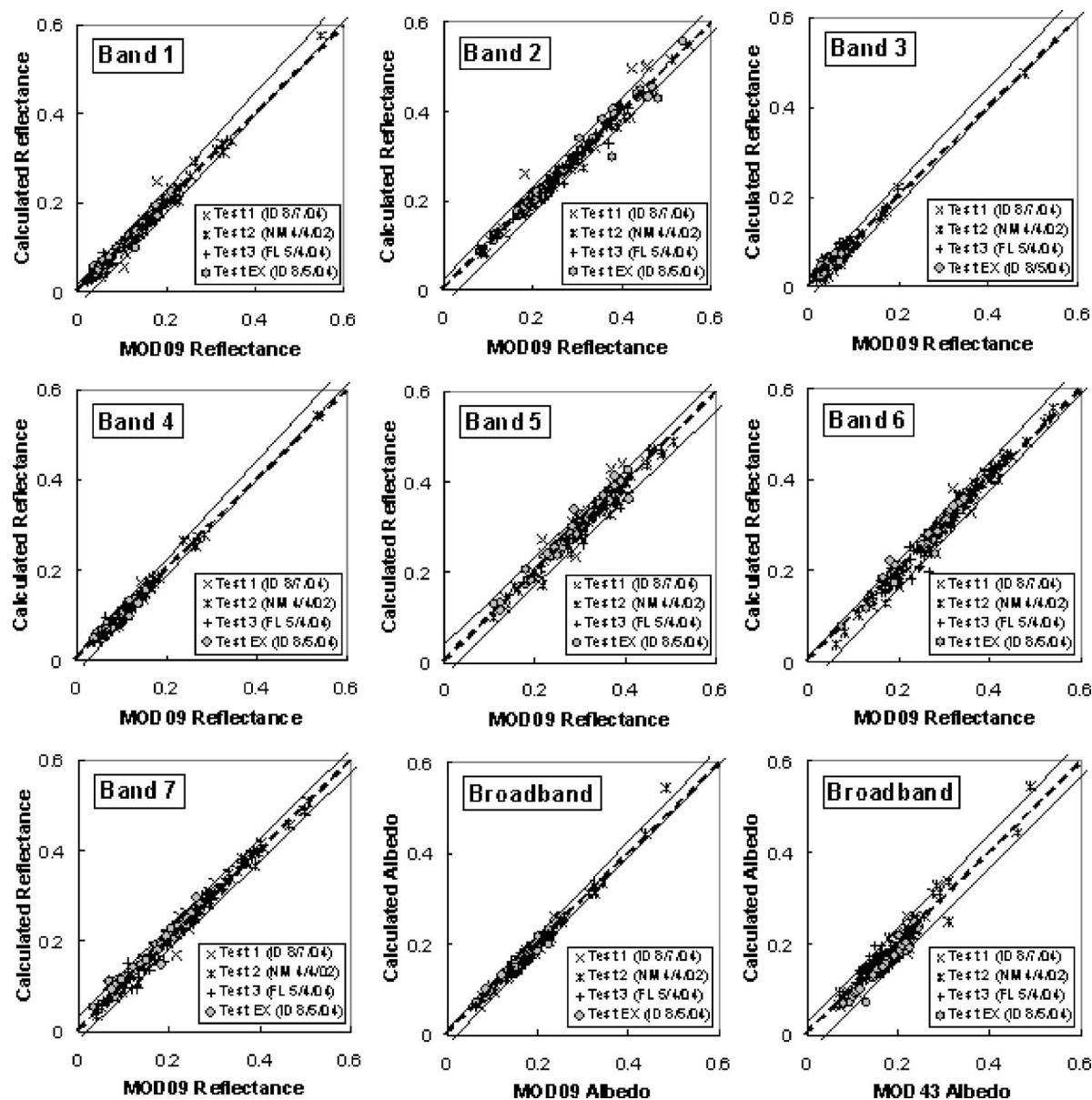


**Fig. 5.** Estimated at-surface reflectance for a MODIS Terra image for three test applications over Idaho (ID), New Mexico (NM), and Florida (FL) and one extra test at large sensor view angle (Test EX) using MOD02 radiance images with Eqs. (2), (3), (6), and (7), compared with the corresponding MODIS Level 2 surface reflectance and Level 3 (MOD09 and MOD43) albedo products. The dotted line is the 1:1 relation and solid lines are the limits for 95% prediction confidence computed for the three normal test applications together (150 samples).

reflectance, which is traceable to the 6S and MODTRAN atmospheric correction models, in both dry and humid climates.

In the broadband level, our estimation closely reproduced at surface broadband albedo as computed from the MOD09 reflectance products (Fig. 5), estimating within  $-0.013$  and  $+0.018$  of the MOD09 albedo (95% CI) over the test applications in Idaho, New Mexico, and Florida. Estimated albedo compared well with the MOD09 derived product even for the application having sensor view angles of  $35\text{--}42^\circ$  (results plotted in Fig. 5), since both estimates are predominately bidirectional. The good agreement for all test applications indicates that the developed reflectance and albedo estimation equations and calibrated coefficients are robust in application, and can be used to estimate the predominately bidirectional surface albedo (i.e., non-BRDF corrected) accurately over a wide range of atmospheric conditions and sensor angles.

The comparisons with the 16-day MOD43 albedo product, which is corrected for BRDF and is composited from as many as 16 daily images, showed larger differences. Compared with MOD43, our estimation fell within  $-0.035$  to  $+0.033$  (95% CI at albedo intensities of  $\approx 0.2$ ), representing a standard error of 0.017 over the three test applications. Some of this error stems from estimation error by our model, which uses a single directional sensor angle (i.e., a single image having near-nadir view angle) whereas, actual surface albedo can have a large directional distribution with view angle. Other differences may stem from error in the MOD43 product including BRDF corrections, and from time and resolution inconsistencies between two products [i.e., instantaneous versus 16-day average and resolution of 500 m versus 1 km (effectively  $2\text{ km} \times 3\text{ km}$  due to view angle induced smearing)].

The estimation error in our albedo algorithm is not well quan-

**Table 7.** Slope and Intercepts of Linear Regression Lines for Calculated and Official MODIS Band Reflectance and Broadband Albedo-Parthesized Values Are Intercepts

| Image number                   | Description              | Band 1         | Band 2         | Band 3         | Band 4         | Band 5         | Band 6         | Band 7        | BB (MOD09)     | BB (MOD43)     |
|--------------------------------|--------------------------|----------------|----------------|----------------|----------------|----------------|----------------|---------------|----------------|----------------|
| 1                              | Calibration <sup>a</sup> | —              | —              | —              | —              | —              | —              | —             | —              | —              |
| 2                              | Test 1 (ID)              | 1.083 (−0.010) | 1.020 (−0.001) | 1.061 (−0.007) | 1.047 (−0.006) | 1.001 (0.002)  | 1.53 (−0.014)  | 0.950 (0.018) | 1.024 (−0.004) | 1.039 (−0.019) |
|                                | ( $r^2$ )                | 0.914          | 0.972          | 0.891          | 0.931          | 0.924          | 0.934          | 0.951         | 0.966          | 0.906          |
| 3                              | Test 2 (NM)              | 1.114 (−0.019) | 1.008 (−0.002) | 1.083 (−0.05)  | 1.096 (−0.012) | 0.975 (0.005)  | 1.060 (−0.015) | 0.990 (0.007) | 1.051 (−0.008) | 1.048 (−0.008) |
|                                | ( $r^2$ )                | 0.983          | 0.985          | 0.989          | 0.988          | 0.968          | 0.989          | 0.991         | 0.985          | 0.948          |
| 4                              | Test 3 (FL)              | 0.936 (0.004)  | 1.014 (−0.003) | 1.174 (0.009)  | 0.968 (0.008)  | 0.992 (−0.001) | 0.969 (−0.004) | 0.896 (0.017) | 0.945 (0.012)  | 1.082 (−0.001) |
|                                | ( $r^2$ )                | 0.909          | 0.981          | 0.904          | 0.912          | 0.936          | 0.894          | 0.891         | 0.934          | 0.723          |
| 5                              | Test EX <sup>b</sup>     | 0.993 (0.004)  | 0.962 (0.011)  | 0.869 (0.011)  | 0.902 (0.011)  | 0.995 (0.004)  | 1.010 (0.000)  | 0.943 (0.022) | 0.951 (0.011)  | 1.017 (−0.020) |
|                                | ( $r^2$ )                | 0.966          | 0.978          | 0.807          | 0.944          | 0.961          | 0.966          | 0.965         | 0.976          | 0.932          |
| Average of Tests 1–3 ( $r^2$ ) |                          | 1.071 (−0.008) | 1.012 (−0.001) | 1.045 (0.000)  | 1.064 (−0.005) | 0.975 (0.007)  | 1.071 (−0.021) | 0.980 (0.010) | 1.032 (−0.004) | 1.022 (−0.008) |
|                                |                          | 0.981          | 0.976          | 0.971          | 0.984          | 0.948          | 0.974          | 0.985         | 0.983          | 0.919          |

<sup>a</sup>Intercept was forced to be 0.00 and slope was forced to be 1.00 during calibration (See Fig. 3).

<sup>b</sup>Text EX is a test for off sensor zenith angle (35–42°, which is significantly more than the application limit of 20°).

tified from the comparison with MOD43 albedo for these reasons and given the relatively small number of test applications. However, the randomness of differences between the two albedo estimates (our model versus MOD43) indicates that the differences are primarily caused by time inconsistencies between the two albedo products (i.e., instantaneous versus 16-day average). In typical Landsat and MODIS-based surface energy balance applications, 0.03 error in the surface albedo estimation causes less than 2% error in net radiation calculations. Therefore, we conclude that our developed albedo algorithm provides albedo with sufficient accuracy for use in surface energy balance studies that estimate spatial distribution of ET, such as the METRIC model (Allen et al. 2007b).

### Comparison of the Integration Procedures for Broadband At-Surface Albedo with Liang (2000)

The weighting coefficients,  $w_b$ , used in this study for integrating reflectances into broadband albedo were derived for use with at-surface solar radiation under standard atmospheric conditions. Broadband albedo estimated using our  $w_b$  values were compared to albedo estimated using weighting coefficients derived by Liang (2000) using regression. Comparisons were made for a Landsat Path 40 Row 30 in southern Idaho acquired August 22, 2000. Fig. 6 shows comparisons for 250 randomly sampled pixels that included irrigated agriculture, bare soil, city, water, desert, basalt rock, and salt-encrusted surfaces. The same at-surface band reflectances were applied for both sets of calculations, thus, the differences in computed albedo between the two methods are purely due to differences in  $w_b$ . The two independently produced sets for  $w_b$  produced essentially identical results for nearly all sampled pixels. However, results systematically deviated for green agricultural fields having high values for the normalized difference vegetation index (NDVI). Differences at high NDVI were caused by the omission of the green band by Liang. It appears that our theoretically based method for band integration provides better estimates for surface albedo for the dense, green agricultural condition. Some random deviation between results from the two weighting methods was observed over extremely bright surfaces having albedo greater than about 0.4. The scatter indicates some uncertainty in accuracy of estimates by either methods under these extreme conditions. The overall agreement between albedo estimates supports the consistency of the weight-

ing coefficients developed by us and by Liang. A primary benefit of our weighting coefficients stems from their derivation based on Equation (8) that allows a new set of coefficients to be derived when a band is missing from an image due to corruption, such as shown in Fig. 1. In this case, new coefficients are readily derived using the information in Table 5 by assigning one-half the value of the coefficient for the missing band to the coefficients of the bands on either side of the missing band. Table 1 provides the spectral order of band numbers for the Landsat and MODIS satellites.

### Combined Comparison of Atmospheric Correction and Integration Coefficients with the EWRI General Transmissivity Model

The development of the simple atmospheric correction algorithms for individual satellite sensor bands relied substantially on the SMARTS2 model and developed equations closely reproduce the SMARTS2 estimates over wide ranges of solar zenith angle, ground elevation and precipitable water for the standard profile conditions, as was shown in Figure 2. As an independent assessment of SMARTS2, simulations of transmittance by SMARTS2

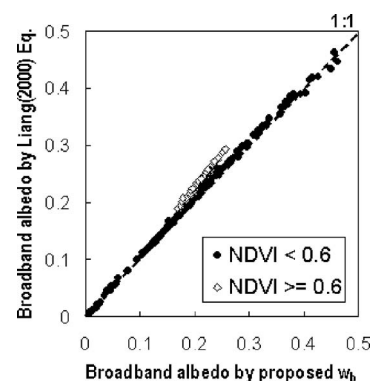


**Fig. 6.** Estimated broadband albedo using integration functions by Liang (2000) versus those from Eq. (7) and Table 5 for an August 22, 2000, Landsat image in southern Idaho for irrigated agriculture, bare soil, city, water, desert, dark basalt rock, and bright salt-encrusted surfaces

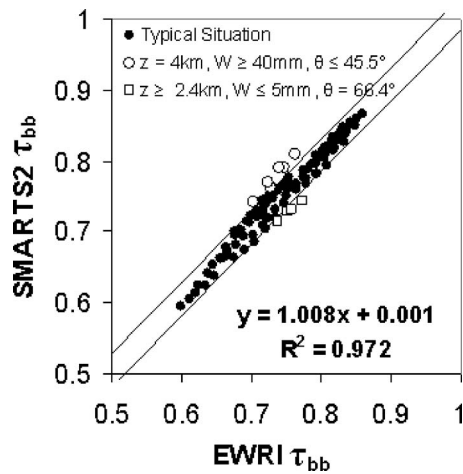


**Fig. 7.** Comparison between broadband transmittance from SMARTS2 and EWRI for 100 combinations of weather and geometric conditions described in Table 5. The regression line and the 95% prediction confidence intervals (shown as solid lines) are for typical situations only.

were compared, in terms of broadband transmittance integrated over the 0.3 to 4.0  $\mu\text{m}$  range, with the broadband transmittance equation of EWRI (2005), which was calibrated using global pyranometer measurements from 49 quality-controlled agricultural weather stations located across the United States (Itensu et al. 2003; EWRI 2005). Results of this comparison are shown in Fig. 7 where estimated transmittances from the two independent methods agreed well over the same 100 combinations of location elevation, precipitable water, and sun angle as used in development of the narrow band transmittance functions. SMARTS2 broadband transmittance values averaged only 1% higher than those by the EWRI equation, with a standard error of 0.017. Data points having significantly different values between the two methods occurred only for extreme sets of conditions; for example, at 4,000 m elevation, with extremely high precipitable water, as shown in Fig. 7. These extreme conditions are probably outside the valid range of the EWRI equation. The close agreement between the two independent calculations indicates that SMARTS2 transmittances reproduce empirically observed transmittances over wide ranges in location and climate as represented by the 49 weather stations at the broadband level. These findings indirectly imply accuracy of spectral transmittances estimated by SMARTS2 and in turn, accuracy of the narrow band transmittance equations and integrated weighting functions developed in this study. The close agreement also indicates that the weighting of the atmospheric pressure and precipitable water terms of the EWRI (2005) equation is appropriate.

### Testing of the Path Reflectance Coefficients

Calculated atmospheric path reflectance,  $\rho_{a,b}$ , as determined during this study from MODIS data products was, to some degree, independently evaluated using the MODTRAN radiative transfer model. The evaluation was made under Idaho summer conditions and differences between path reflectances calculated by our calibrated Equation (9) and derived from MODTRAN are summarized in Table 8. Path reflectances were isolated from MODTRAN runs by dividing out transmittance estimated using Eqs. (3) and (6). Differences between the two methods were small, ranging as high as 0.024 in some narrow bands and less than 0.006 on a broadband basis. These differences are considered to be within accuracy tolerances for estimating surface albedo and they indicate similarities in path reflectance from two mostly independent atmospheric correction models (MODTRAN and that used in MODIS products). The path reflectance values from our calibrated model, when integrated using Eq. (7), are close to literature values of 0.035–0.038 determined by Bastiaanssen (2000) in Turkey and 0.030 determined by Tasumi (2003) in Idaho using known dark objects from Landsat satellite images.

### Conclusions

We present a surface albedo estimation method that can be applied to Landsat and MODIS imagery for deriving at-surface albedo from near-nadir sensor view angles for use in energy balance determination of ET. The developed method was calibrated using the SMARTS2 radiative transfer model for atmospheric transmittance and MODIS surface reflectance products for atmospheric path reflectance. The method is composed of simplified, explicit equations, with a data requirement of air-humidity and digital elevation model (DEM) only. Therefore, the method can be utilized in operational and routine applications with satellite imagery to estimate incoming and outgoing atmospheric transmittance for low haze, cloud free conditions. Although the method is applicable for nonnadir images, the estimation accuracy of at-surface reflectance degrades as sensor view angle increases due to the lack of consideration of BRDF. A maximum sensor view angle of  $20^\circ$  is recommended in the absence of BRDF correction. This is not a concern with Landsat images that are always near nadir.

The developed method was tested and compared against MODIS at-surface reflectance and albedo products (MOD09 and MOD43), against a general broadband transmittance equation calibrated using solar radiation data from 49 U.S. locations, and against literature values. Although robust validations using actual ground-based measurements have not been conducted, the results of the comparisons indicate good estimation accuracy ( $\pm 0.035$  maximum error in actual surface albedo and  $\pm 0.018$  for bidirec-

**Table 8.** Comparison between MODIS Calibrated and MODTRAN Calibrated Path Reflectance

| Bands   |            | Band 1 | Band 2 | Band 3 | Band 4 | Band 5 | Band 6 | Band 7 | Average <sup>a</sup> |
|---------|------------|--------|--------|--------|--------|--------|--------|--------|----------------------|
| Landsat | Calibrated | 0.079  | 0.043  | 0.027  | 0.011  | 0.012  | —      | −0.012 | 0.035                |
|         | MODTRAN    | 0.073  | 0.060  | 0.034  | 0.019  | 0.018  | —      | 0.015  | 0.041                |
| MODIS   | Calibrated | 0.027  | 0.009  | 0.087  | 0.042  | 0.005  | 0.014  | −0.012 | 0.036                |
|         | MODTRAN    | 0.032  | 0.008  | 0.063  | 0.032  | 0.001  | 0.003  | 0.009  | 0.030                |

Note: Expressed in units of reflectance (dimensionless).

<sup>a</sup>Weighted average calculated by  $w_b$  in Table 6.

**Table 9.** Mean Solar Exoatmospheric Spectral Radiation,  $ESUN_b$  ( $W m^{-2} \mu m^{-1}$ ), for Landsat and MODIS

| Band | Landsat 4 <sup>a</sup> | Landsat 5 <sup>a</sup> | Landsat 7 <sup>b</sup> | MODIS <sup>c</sup> |
|------|------------------------|------------------------|------------------------|--------------------|
| 1    | 1,957                  | 1,957                  | 1,969                  | 1,596              |
| 2    | 1,825                  | 1,826                  | 1,840                  | 974.7              |
| 3    | 1,557                  | 1,554                  | 1,551                  | 2,017              |
| 4    | 1,033                  | 1,036                  | 1,044                  | 1,850              |
| 5    | 214.9                  | 215.0                  | 225.7                  | 463.1              |
| 6    | —                      | —                      | —                      | 232.9              |
| 7    | 80.72                  | 80.67                  | 82.07                  | 92.67              |
| 8    | —                      | —                      | 1368                   | —                  |

<sup>a</sup>Chander and Markham (2003).

<sup>b</sup>LPSO (2006).

<sup>c</sup>Calculated using the SMARTS2 (Gueymard 1995) spectral  $ESUN$  data set and MODIS band sensor response.

tional albedo at 95% confidence) for use in operational applications of land surface energy balance models. The transmittance equation calibrated in this study closely reproduced the transmittance simulated by the SMARTS2 radiative transfer model and corresponds well with the EWRI (2005) broadband transmittance method. The calibrated atmospheric path reflectances agreed well with an independent test using MODTRAN and also with literature values. The theoretical weighting coefficients used to integrate band reflectances to broadband albedo agree well with the independently derived method of Liang (2000). The procedure presented in this paper is applicable to other satellite sensors for development of specific coefficients for Eqs. (3) and (6) and weighting coefficients for Eq. (7).

## Appendix. Calculation of At-Satellite Bidirectional Reflectance

The digital number (DN) of a Landsat image is convertible to radiance ( $W m^{-2} sr^{-1} \mu m^{-1}$ ) using the method and calibration coefficients described in Chander and Markham (2003) for Landsat 5 and LPSO (2006) for Landsat 7. MODIS (MOD02 Level 1b) image contains the calibration numbers in the header information of the image.

At-satellite (BD) band reflectance,  $\rho_{t,b}$  is calculated from at-satellite directional radiance as

$$\rho_{t,b} = \frac{\pi \cdot L_{t,b} \cdot d^2}{ESUN_b \cdot \cos \theta_{rel}} \quad (10)$$

where  $L_{t,b}$ =at-satellite spectral radiance in band  $b$  ( $W m^{-2} sr^{-1} \mu m^{-1}$ );  $ESUN_b$ =mean solar exoatmospheric radiation over band  $b$  ( $W m^{-2} \mu m^{-1}$ ) given in Table 9,  $\theta_{rel}$ =solar incident angle (or solar zenith angle) relative to the land surface slope; and  $d$ =earth-sun distance in astronomical units.

Parameter  $d^2$  can be calculated as a function of day of year using Duffie and Beckman (1991)

$$d^2 = \frac{1}{1 + 0.033 \cos(DOY \cdot 2\pi/365)} \quad (11)$$

where  $DOY$ =day of year and  $(DOY \cdot 2\pi/365)$  (rad).

The solar incidence angle is the angle between the solar beam and a vertical line perpendicular to the land surface. For horizontal flat surfaces,  $\theta_{rel}$  is simply equivalent to solar zenith angle (i.e.,  $\pi/2$  minus the solar elevation angle). However, for sloping surfaces,  $\theta_{rel}$  must be calculated pixel by pixel, using surface slope

and aspect information derived from a digital elevation model or other means using the following equation (Duffie and Beckman 1991):

$$\begin{aligned} \cos \theta_{rel} = & \sin(\delta)\sin(\phi)\cos(s) - \sin(\delta)\cos(\phi)\sin(s)\cos(\gamma) \\ & + \cos(\delta)\cos(\phi)\cos(s)\cos(\omega) \\ & + \cos(\delta)\sin(\phi)\sin(s)\cos(\gamma)\cos(\omega) \\ & + \cos(\delta)\sin(s)\sin(\gamma)\sin(\omega) \end{aligned} \quad (12)$$

where  $\delta$ =declination of the earth (positive in summer in the northern hemisphere);  $\phi$ =latitude of the pixel (positive for the northern hemisphere and negative for the southern hemisphere);  $s$ =surface slope where  $s=0$  for horizontal and  $s=\pi/2$  rad for vertical downward slope ( $s$  is always positive and represents the downward slope in any direction); and  $\gamma$ =surface aspect angle, where  $\gamma=0$  for slopes oriented due south,  $\gamma=-\pi/2$  rad for slopes oriented due east,  $\gamma=+\pi/2$  rad for slopes oriented due west and  $\gamma=\pm\pi$  rad for slopes oriented due north. Parameter  $\omega$  is the hour angle, where  $\omega=0$  at solar noon,  $\omega$  is negative in morning and  $\omega$  is positive in afternoon following the convention of Duffie and Beckman (1991).

## References

- Allen, R. G., Pereira, L. S., Raes, D., and Smith, M. (1998). "Crop evapotranspiration." *FAO Irrigation and drainage Paper*, 56, FAO, Rome, Italy.
- Allen, R. G., Tasumi, M., Morse, A., and Trezza, R. (2005). "A Landsat-based energy balance and evapotranspiration model in western U.S. water rights regulation and planning." *J. Irrig. Drain. Sys.*, 19, 251–268.
- Allen, R. G., Tasumi, M., Morse, A., Trezza, R., Wright, J. L., Bastiaansen, W., Kramber, W., Lorite, I., and Robison, C. W. (2007a). "Satellite-based energy balance for mapping evapotranspiration with internalized calibration (METRIC)—Applications." *J. Irrig. Drain. Eng.*, 133(4), 395–406.
- Allen, R. G., Tasumi, M., and Trezza, R. (2007b). "Satellite-based energy balance for mapping evapotranspiration with internalized calibration (METRIC)—Model." *J. Irrig. Drain. Eng.*, 133(4), 380–394.
- Anderson, G. P., Clough, S. A., Kneizys, F. X., Chetwynd, J. H., and Shettle, E. P. (1986). "AFGL atmospheric constituent profiles (0–120 km)." *Technical Rep. AFGL-TR-86-0110*, Air Force Geophysics Laboratory, Hanscom AFB, Mass.
- Bastiaansen, W. G. M. (2000). "SEBAL-based sensible and latent heat fluxes in the irrigated Gediz Basin, Turkey." *J. Hydrol.*, 229, 87–100.
- Bastiaansen, W. G. M., Menenti, M., Feddes, R. A., and Holtslag, A. A. M. (1998). "A remote sensing surface energy balance algorithm for land (SEBAL): 1. Formulation." *J. Hydrol.*, 212–213, 198–212.
- Bastiaansen, W. G. M., Noordman, E. J. M., Pelgrum, H., Davids, G., Thoreson, B. P., and Allen, R. G. (2005). "SEBAL model with remotely sensed data to improve water-resources management under actual field conditions." *J. Irrig. Drain. Eng.*, 131(1), 85–93.
- Ben-Dor, E., Kindel, B., and Goetz, A. F. H. (2004). "Quality assessment of several methods to recover surface reflectance using synthetic imaging spectroscopy data." *Remote Sen. Environ.*, 90, 389–404.
- Berk, A., et al. (1999). "MODTRAN4 radiative transfer modeling for atmospheric correction." *Proc. SPIE Optical Spectroscopic Techniques and Instrumentation for Atmospheric and Space Research III*, 3756.
- Berthouex, P. M., and Brown, L. C. (1994). *Statistics for environmental engineers*, Lewis, Boca Raton, Fla.
- Chander, G., and Markham, B. (2003). "Revised Landsat-5 TM radiometric calibration procedures and postcalibration dynamic ranges." *IEEE Trans. Geosci. Remote Sens.*, 41(11), 2674–2677.



- Chavez, P. S., Jr. (1988). "An improved dark-object subtraction technique for atmospheric scattering correction of multispectral data." *Remote Sens. Environ.*, 24, 459–479.
- Chavez, P. S., Jr. (1996). "Image-based atmospheric corrections—Revised and improved." *Photogramm. Eng. Remote Sens.*, 62, 1025–1036.
- Duffie, J. A., and Beckman, W. A. (1991). *Solar engineering of thermal process*, 2nd Ed., Wiley, New York.
- EWRI Task Committee on Standardization of Reference Evapotranspiration of the Environmental and Water Resources Institute of the ASCE (EWRI). (2005). *The ASCE standardized reference evapotranspiration equation*, R. G. Allen et al., eds., ASCE, Reston, Va.
- Farah, H. O., and Bastiaanssen, W. G. M. (2001). "Impact of spatial variations of land surface parameters on regional evaporation: A case study with remote sensing data." *Hydrolog. Process.*, 15, 1585–1607.
- Gao, B.-C., and Kaufman, Y. J. (1999). "The MODIS near IR water vapor algorithm." *MODIS algorithm theoretical background document*, ([http://modis-atmos.gsfc.nasa.gov/\\_docs/atbd\\_mod03.pdf](http://modis-atmos.gsfc.nasa.gov/_docs/atbd_mod03.pdf)).
- Garrison, J. D., and Adler, G. P. (1990). "Estimation of precipitable water over the United States for application to the division of solar radiation into its direct and diffuse components." *Sol. Energy*, 44(4), 225–241.
- Gueymard, C. (1995). "SMARTS2, a simple model of the atmospheric radiative transfer of sunshine: Algorithms and performance assessment." *Professional Paper FSEC-PF-270-95*, Florida Solar Energy Center, Univ. of Central Florida, Cocoa, Fla.
- Itenfisu, D., Elliott, R. L., Allen, R. G., and Walter, I. A. (2003). "Comparison of reference evapotranspiration calculations as part of the ASCE standardization effort." *J. Irrig. Drain. Eng.*, 129(6), 440–448.
- Jia, L., et al. (2003). "Estimation of sensible heat flux using the surface energy balance system (SEBS) and ATSR measurements." *Phys. Chem. Earth, Part B*, 28, 75–88.
- Kramber, W. J. (2002). *Developing evapotranspiration data for Idaho's Treasure Valley using surface energy balance algorithm for land (SEBAL)*, Idaho Dept. of Water Resources, Boise, Idaho.
- Landsat, Project Science Office (LPSO). (2006). *Landsat 7 science data users' handbook*, Landsat Project Science Office, NASA Goddard Space Flight Center, Greenbelt, Md., ([http://ltpwww.gsfc.nasa.gov/IAS/handbook/handbook\\_toc.html](http://ltpwww.gsfc.nasa.gov/IAS/handbook/handbook_toc.html)) (Nov. 15, 2006).
- Liang, S. (2000). "Narrowband to broadband conversions of land surface albedo. I: Algorithms." *Remote Sensing Environ.*, 76, 213–238.
- Liang, S., et al. (2002a). "Atmospheric correction of Landsat ETM+ land surface imagery—Part II: Validation and applications." *IEEE Trans. Geosci. Remote Sens.*, 40(12), 2737–2746.
- Liang, S., et al. (2002b). "Validating MODIS land surface reflectance and albedo products: Methods and preliminary results." *Remote Sensing Environ.*, 83, 149–162.
- Liang, S., Fang, H., and Chen, M. (2001). "Atmospheric correction of Landsat ETM+ land surface imagery—Part I: Methods." *IEEE Trans. Geosci. Remote Sens.*, 39, 2490–2498.
- Ma, Y., Menenti, M., Tsukamoto, O., Ishikawa, H., Wang, J., and Gao, Q. (2004). "Remote sensing parametrization of regional land surface heat fluxes over arid area in northwestern China." *J. Arid Environ.*, 57(2), 257–273.
- Majumdar, N. C., Mathur, B. L., and Kaushik, S. B. (1972). "Prediction of direct solar radiation for low atmospheric turbidity." *Sol. Energy*, 13, 383–394.
- Moran, M. S., Bryant, R., Thome, K., Ni, W., Nouvellon, Y., and Gonzalez-Dugo, M. P. (2001). "A refined empirical line approach for reflectance factor retrieval from Landsat-5 TM and Landsat-7 ETM+." *Remote Sensing Environ.*, 78, 71–82.
- NASA. (2005). "MODIS land quality assessment—Known product issues." Internet article, ([http://modland.nascom.nasa.gov/cgi-bin/QA\\_WWW/newPage.cgi](http://modland.nascom.nasa.gov/cgi-bin/QA_WWW/newPage.cgi)) (June 19, 2005).
- National Oceanic and Atmospheric Administration, National Aeronautics and Space Administration, and United States Air Force (NOAA/NASA/USAF). (1976). *U.S. standard atmosphere, 1976*, U.S. Government Printing Office, Washington, D.C.
- Roerink, G. J., Su, Z., and Menenti, M. (2000). "S-SEBI: A simple remote sensing algorithm to estimate the surface energy balance." *Phys. Chem. Earth, Part B*, 25(2), 147–157.
- Schaaf, C., et al. (2002). "First operational BRDF, albedo and nadir reflectance products from MODIS." *Remote Sens. Environ.*, 83, 135–148.
- Smith, G. M., and Milton, E. J. (1999). "The use of the empirical line method to calibrate remotely sensed data to reflectance." *Int. J. Remote Sens.*, 20(13), 2653–2662.
- Starks, P. J., Norman, J. M., Blad, B. L., Walter-Shea, E. A., and Walthall, C. L. (1991). "Estimation of shortwave hemispherical reflectance (albedo) from bidirectionally reflected radiance data." *Remote Sens. Environ.*, 38, 123–134.
- Staenz, K., Secker, J., Gao, B.-C., Davis, C., and Nadeau, C. (2002). "Radiative transfer codes applied to hyperspectral data for the retrieval of surface reflectance." *ISPRS J. Photogramm. Remote Sens.*, 57, 194–203.
- Su, Z. (2002). "The surface energy balance system (SEBS) for estimation of turbulent heat fluxes." *Hydrology Earth Syst. Sci.*, 6(1), 85–99.
- Tasumi, M. (2003). "Progress in operational estimation of regional evapotranspiration using satellite imagery." Ph.D. dissertation, Univ. of Idaho, Moscow, Idaho.
- Tasumi, M., Allen, R. G., and Bastiaanssen, W. G. M. (2000). "The theoretical basis of SEBAL." *Application of the SEBAL Methodology for Estimating Consumptive Use of Water and Streamflow Depletion in the Bear River Basin of Idaho through Remote Sensing: Final Rep.*, Idaho Dept. of Water Resources, Idaho.
- Tasumi, M., Trezza, R., Allen, R. G., and Wright, J. L. (2005). "Operational aspects of satellite-based energy balance models for irrigated crops in the semi-arid U.S." *J. Irrig. Drain. Sys.*, 19, 355–376.
- Teillet, P. M., and Fedosejevs, G. (1995). "On the dark target approach to atmospheric correction of remotely sensed data." *Can. J. Remote Sens.*, 21(4), 374–387.
- Vermote, E. F., Tanre, D., Deuze, J. L., Herman, M., and Morcrette, J. J. (1997). "Second simulation of the satellite signal in the solar spectrum: An overview." *IEEE Trans. Geosci. Remote Sens.*, 35, 3.
- Vermote, E. F., and Vermeulen, A. (1999). "Atmospheric correction algorithm: Spectral reflectances (MOD09)." *MODIS algorithm theoretical background document*, ([http://modis.gsfc.nasa.gov/data/atbd/atbd\\_mod09.pdf](http://modis.gsfc.nasa.gov/data/atbd/atbd_mod09.pdf)).
- Wen, G., Tsay, S.-C., Cahalan, R. F., and Oreopoulos, L. (1999). "Path radiance technique for retrieving aerosol optical thickness over land." *J. Geophys. Res.*, 104(D24), 31321–31332.
- Zhao, W., Tamura, M., and Takahashi, H. (2000). "Atmospheric and spectral corrections for estimating surface albedo from satellite data using 6S code." *Remote Sensing Environ.*, 76, 202–212.

Copyright of Journal of Hydrologic Engineering is the property of American Society of Civil Engineers and its content may not be copied or emailed to multiple sites or posted to a listserv without the copyright holder's express written permission. However, users may print, download, or email articles for individual use.

Copyright of Journal of Hydrologic Engineering is the property of American Society of Civil Engineers and its content may not be copied or emailed to multiple sites or posted to a listserv without the copyright holder's express written permission. However, users may print, download, or email articles for individual use.